

Photoemission tomography of excitons in 2D systems: momentum-space signatures of correlated electron-hole wave functions

Siegfried Kaidisch,¹ Amir Kleiner,² Sivan Refaelly-Abramson,² Peter Puschnig,¹ and Christian S. Kern^{1,*}

¹*Institute of Physics, NAWI Graz, University of Graz, 8010 Graz, Austria*

²*Department of Molecular Chemistry and Materials Science,*

Weizmann Institute of Science, Rehovot, 7610001, Israel

(Dated: November 20, 2025)

The momentum-space signatures of excitons can be experimentally accessed through time-resolved (pump-probe) photoelectron spectroscopy. In this work, we develop a computational framework for exciton photoemission orbital tomography (exPOT) in periodic systems, enabling the simulation and interpretation of experimental observables within many-body perturbation theory. By connecting the GW +Bethe-Salpeter Equation (BSE) approach to photoemission tomography, our formalism captures exciton photoemission in periodic systems, explicitly incorporating photoemission matrix element effects induced by the probe pulse. The correlated nature of electrons and holes introduces distinct consequences for excitonic photoemission, including a dependence on pump pulse polarization. Using the prototypical two-dimensional material hexagonal boron nitride, we demonstrate these effects and show how our framework extends to excitons with finite center-of-mass momentum, making it well-suited to studying momentum-dark excitons. This provides valuable insights into the microscopic nature of excitonic phenomena in quantum materials.

I. INTRODUCTION

Excitons—bound electron-hole pairs—play a fundamental role in determining the optical and electronic response of semiconducting and insulating (two-dimensional) materials. From a theoretical perspective, describing excitonic effects requires going beyond single-particle approximations and typically involves time-dependent density functional theory (TDDFT) with suitable long-range xc-kernels, or many-body perturbation theory (MBPT) within the GW plus Bethe-Salpeter equation (BSE) framework [1–3]. Excitation energies and optical spectra computed in such a way can then be compared to absorption or luminescence spectroscopy. While theory naturally provides detailed information about the quantum mechanical nature of the exciton wave function in real and momentum space, optical experiments provide only limited microscopic insights.

Here, time- and angle-resolved photoemission spectroscopy (trARPES) has emerged as a promising tool to dynamically probe excited states in energy and momentum space, thus offering enhanced insight into the microscopic nature of excitons [4–10]. It is therefore highly desirable to have a theory that can connect trARPES signature with first-principles calculations. The arguably most direct way of simulating trARPES is a numerical photodetection scheme, as implemented in real-time TDDFT [11, 12], which not only allows for pump-probe simulations in linear and nonlinear regimes but also captures final-state effects in the photoemission process [13, 14]. Unfortunately, non-equilibrium approximation for the xc-kernel in real-time TDDFT is the adiabatic local density approximation, which fails to capture

excitonic effects.

This is in contrast to Green’s function methods, where the inclusion of Coulomb correlation between electron and hole, in conjunction with the screened exchange interaction, successfully describes bound electron-hole states. The non-equilibrium Greens function (NEGF) method is particularly powerful for simulating excited systems through explicit time propagation, capturing the effects of many-body interactions, such as electron-electron and electron-phonon scattering, via self-energy corrections [15]. The photoemission signal is then derived from the lesser Green’s function and the matrix element [16], with the former resulting from the non-equilibrium occupation due to the pump pulse and the latter accounting for the effects of the probe pulse. However, due to the complexity of the method, trARPES simulations within the NEGF framework have so far been restricted to model systems or Wannier Hamiltonians [17, 18], often neglecting the influence of the probe pulse [19, 20].

In one-step models for photoemission, such probe pulse effects are encoded in the photoemission matrix element. Matrix element effects are not only crucial for accurately describing the photoemission process itself, but also encode rich information about quantum geometrical effects [21, 22], such as the Berry curvature [23, 24] or orbital angular momentum [25, 26]. Moreover, in organic or hybrid organic/inorganic systems, matrix element effects may easily become the dominant contribution to the observed angular dependence in the photoemission signal, forming the basis of the successful photoemission orbital tomography (POT) approach [27–29].

For organic molecules, POT has recently been conceptually extended to exciton photoemission orbital tomography (exPOT) [30], which establishes a direct connection between the angular distributions observed in trARPES and the real-space and momentum-space struc-

* email: christian.kern@uni-graz.at

ture of excitonic wave functions. However, this earlier work was limited to non-periodic systems, such as isolated molecules, thereby restricting its applicability to condensed-phase materials and low-dimensional crystals.

In the present work, we introduce exPOT for periodic systems, an ab initio scheme to simulate trARPES from first-principles. In contrast to explicit time-propagation methods, here we work in frequency space and with the exciton wave function from $GW + BSE$ calculations in the linear response regime. The photoemission signal is then expressed in terms of the Fourier-transformed single-particle Bloch functions, weighted by the BSE eigenvectors and thus reflecting the entangled many-body character of electron-hole correlation. Our numerical implementation builds upon any solution of the BSE expressed in a plane wave basis set and is thus suited to treat crystalline solids and 2D semiconductors in the repeated-slab approach. We use the plane wave approximation for the final state in the photoemission process, including effects of the light polarization. In addition, our generalized theory is also able to describe excitons with finite center-of-mass momentum, allowing for the treatment of optically dark excitons—a key feature in transition metal dichalcogenides (TMDs) and other layered materials [8, 31–33]. The exPOT approach in periodic systems thus enables access to a new class of excitonic observables in photoemission, bridging the gap between theoretical many-body wave functions and experimental momentum-resolved spectra.

This work is structured as follows. First we formulate the theoretical foundations in Section II, starting from Fermi’s golden rule for the photoemission process, and including the many-body excitonic effects in terms of a Dyson orbital-like construction for Bloch functions. For energy-degenerate excitons, the resulting expression for photoemission from excitons also carries an additional dependence on the pump polarization, which is discussed thereafter. To exemplify the method, we present results in Section III, where we apply our method to monolayer hexagonal boron nitride (hBN), a prototypical 2D semiconductor with well-characterized excitonic properties. We further show that the resulting photoelectron angular distributions depend not only on the character of the exciton but also on the polarization of the pump pulse, and discuss the implications of our theory on the rich information contained in exciton photoemission.

II. THEORY

A. Derivation of exPOT for periodic systems

In this section, we derive the formalism on which we base our interpretation of photoelectron spectroscopy in terms of exciton wave functions and under the following conditions. First, we assume that the optical excitation (i.e. the pump pulse) is weak, such that we stay in the linear regime and well below the exciton Mott transition

threshold, and that the pump pulse is long enough to minimize energy broadening. Second, we assume that the probe pulse interacts with the system only after the pump pulse has ended. This ensures the preparation of a coherent exciton [34, 35] and avoids energy streaking effects in the trARPES spectrum induced by the pump. Third, we assume a sufficiently long probe time window to achieve adequate energy resolution in the photoelectron spectra.

Assuming a finite band gap, we model the system’s excited state using a correlated electron-hole wavefunction, expressed in terms of single-particle Bloch states as the basis set. To distinguish between electron and hole states, we write the valence states as $\phi_{v,\mathbf{q}}(\mathbf{r})$, with v denoting the band index and \mathbf{q} the crystal momentum. Similarly, conduction states are written as $\xi_{c,\mathbf{q}}(\mathbf{r})$. With these single particle basis sets and assuming the Tamm-Dancoff approximation (TDA), we can write the m -th exciton wave function, $|m, \mathbf{Q}\rangle$, in terms of electron- and hole coordinates, \mathbf{r}_e and \mathbf{r}_h respectively [2]:

$$\langle \mathbf{r} | m, \mathbf{Q} \rangle = \Psi^{(m, \mathbf{Q})}(\mathbf{r}_h, \mathbf{r}_e) = \sum_{\mathbf{q}}^{\text{BZ}} \sum_{v}^{N_{\text{occ}}} \sum_{c}^{\infty} X_{v,c,\mathbf{q}}^{(m, \mathbf{Q})} \phi_{v,\mathbf{q}}^*(\mathbf{r}_h) \xi_{c,\mathbf{q}+\mathbf{Q}}(\mathbf{r}_e). \quad (1)$$

In this expression, \mathbf{Q} represents the center-of-mass momentum of the exciton, and $X_{v,c,\mathbf{q}}^{(m, \mathbf{Q})}$ are the elements of the transition density matrix, which encode the exciton character and oscillator strength. These eigenstates arise from the BSE Hamiltonian or the Casida equation. The m -th excitation energy is further written as $\Omega^{(m, \mathbf{Q})}$. In the language of second quantization, such exciton states may also be written as

$$|\Psi_m^N, \mathbf{Q}\rangle = \sum_{\mathbf{q}}^{\text{BZ}} \sum_{v,c} X_{v,c,\mathbf{q}}^{(m, \mathbf{Q})} \hat{a}_{c,\mathbf{q}+\mathbf{Q}}^\dagger \hat{a}_{v,\mathbf{q}} |\Psi_0^N\rangle. \quad (2)$$

Here, $\hat{a}_{v,\mathbf{q}}$ annihilates an electron with crystal momentum \mathbf{q} in the valence band v (or creates a hole) in the ground state $|\Psi_0^N\rangle$, and $\hat{a}_{c,\mathbf{q}+\mathbf{Q}}^\dagger$ creates an electron in the conduction band c with momentum $\mathbf{q} + \mathbf{Q}$.

In the spirit of ground state POT [29], and under the conditions states above, we treat the photoemission due to the probe pulse in first-order perturbation theory. Specifically, we apply Fermi’s golden rule for the transition rate from an N -electron initial state $|\Psi_i^N\rangle$ to a final state $|\Psi_f^N\rangle$:

$$W_{i \rightarrow f} = 2\pi \left| \langle \Psi_f^N | \mathbf{A} \hat{\mathbf{P}} | \Psi_i^N \rangle \right|^2 \delta(\omega + E_i - E_f), \quad (3)$$

with the Dirac delta function enforcing energy conservation between the initial and final state and the energy ω carried by the photon field \mathbf{A} . Here and in the following, we use the velocity gauge in the dipole approximation and use atomic units unless denoted otherwise.

The final state $|\Psi_f^N\rangle$ describes the system after the photoemission event. Here, we make use of the sudden

approximation [36] and thus neglect correlation between the photoelectron described by the one-electron state $\gamma_{\mathbf{k}}$ and the remaining $N - 1$ -electron state $|\Psi_f^{N-1}\rangle$. Therefore, $|\Psi_f^N\rangle$ can be written as an anti-symmetrized product:

$$|\Psi_f^N\rangle = \hat{\mathcal{A}}(|\Psi_f^{N-1}\rangle \otimes |\gamma_{\mathbf{k}}\rangle) \equiv |\mathcal{A}\Psi_f^{N-1}\gamma_{\mathbf{k}}\rangle, \quad (4)$$

assuming the $N - 1$ -electron final state to be of the form

$$|\Psi_{j,\tilde{\mathbf{q}}}^{N-1}\rangle \equiv \hat{a}_{j,\tilde{\mathbf{q}}}|\Psi_0^N\rangle, \quad (5)$$

where $\hat{a}_{j,\tilde{\mathbf{q}}}$ annihilates an electron (creates a photo-hole) in band j , and with crystal momentum $\tilde{\mathbf{q}}$, from the N -electron ground state $|\Psi_0^N\rangle$.

In the following, we take the m -th excited state with center-of-mass momentum \mathbf{Q} as initial state, and assume that in the final state, the emitted electron has momentum \mathbf{k} , while the photo-hole resides in $|\phi_{j,\tilde{\mathbf{q}}}\rangle$ (or $|\xi_{j,\tilde{\mathbf{q}}}\rangle$, if it were to reside in a conduction band.). Then, the matrix element $\langle \Psi_f^N | \mathbf{A} \hat{\mathbf{P}} | \Psi_i^N \rangle$ of Equation 3 takes the form

$$M_{j,\tilde{\mathbf{q}},\mathbf{k}}^{(m,\mathbf{Q})}(\mathbf{A}) \equiv \langle \mathcal{A}\Psi_{j,\tilde{\mathbf{q}}}^{N-1}\gamma_{\mathbf{k}} | \mathbf{A} \hat{\mathbf{P}} | \Psi_{m,\mathbf{Q}}^N \rangle. \quad (6)$$

Note that with this matrix element we can calculate the transition rate from $|\Psi_{m,\mathbf{Q}}^N\rangle$ to *one* specific final state, $|\mathcal{A}\Psi_{j,\tilde{\mathbf{q}}}^{N-1}\gamma_{\mathbf{k}}\rangle$ where an electron has been removed from the j -th band (and carrying crystal momentum $\tilde{\mathbf{q}}$). To account for all possible photoemission final states, we will have to sum up the transition rates of all final hole quantum numbers at a later stage.

To proceed, we reduce the N -electron matrix element of Equation 6 to an effective one-electron matrix element by utilizing the Dyson orbital as the overlap between the N -electron and the $N - 1$ -electron system [37–39]. In contrast to existing literature for isolated systems, we here perform this step for many-body Bloch functions that carry an additional crystal momentum quantum number. To see that this is indeed possible, one can always transform Bloch functions with a finite sampling of the Brillouin-zone to a supercell. We then get for the absolute of the matrix element

$$\left| M_{j,\tilde{\mathbf{q}},\mathbf{k}}^{(m,\mathbf{Q})}(\mathbf{A}) \right| = \left| \int_V d^3r \gamma_{\mathbf{k}}^*(\mathbf{r}) \mathbf{A} \nabla D_{j,\tilde{\mathbf{q}}}^{(m,\mathbf{Q})}(\mathbf{r}) \right|, \quad (7)$$

using the effective single-particle Bloch-Dyson state:

$$D_{j,\tilde{\mathbf{q}}}^{(m,\mathbf{Q})}(\mathbf{r}) = \sqrt{N} \int_V d^3r_2 \dots d^3r_N \langle \Psi_{j,\tilde{\mathbf{q}}}^{N-1} | \mathbf{r}_2, \dots, \mathbf{r}_N \rangle \cdot \langle \mathbf{r}, \mathbf{r}_2, \dots, \mathbf{r}_N | \Psi_{m,\mathbf{Q}}^N \rangle. \quad (8)$$

Here the volume of integration, V , is the volume of the unit cell, for which we assume a sampling of the Brillouin zone in the periodic direction only, as well as sufficient vacuum in the non-periodic direction of the slab.

Next we can evaluate the formal definition of the Dyson wave function in the basis of valence- and conduction

bands (see Appendix A for a derivation of this expansion):

$$D_{j,\tilde{\mathbf{q}}}^{(m,\mathbf{Q})}(\mathbf{r}) = \sum_{v'} \sum_{\mathbf{q}'}^{\text{BZ}} \langle \Psi_{j,\tilde{\mathbf{q}}}^{N-1} | \hat{a}_{v',\mathbf{q}'} \rangle \langle \Psi_{m,\mathbf{Q}}^N | \phi_{v',\mathbf{q}'}(\mathbf{r}) \rangle + \sum_{c'} \sum_{\mathbf{q}'}^{\text{BZ}} \langle \Psi_{j,\tilde{\mathbf{q}}}^{N-1} | \hat{a}_{c',\mathbf{q}'} \rangle \langle \Psi_{m,\mathbf{Q}}^N | \xi_{c',\mathbf{q}'}(\mathbf{r}) \rangle. \quad (9)$$

Inserting Equation 2 and Equation 5, we get:

$$\begin{aligned} D_{j,\tilde{\mathbf{q}}}^{(m,\mathbf{Q})}(\mathbf{r}) &= \\ &= \sum_{v',c} \sum_{\mathbf{q},\mathbf{q}'}^{\text{BZ}} X_{v,c,\mathbf{q}}^{(m,\mathbf{Q})} \langle \Psi_0^N | \hat{a}_{j,\tilde{\mathbf{q}}}^\dagger \hat{a}_{v',\mathbf{q}'} \hat{a}_{c,\mathbf{q}+\mathbf{Q}}^\dagger \hat{a}_{v,\mathbf{q}} | \Psi_0^N \rangle \phi_{v',\mathbf{q}'}(\mathbf{r}) \\ &+ \sum_{v,c,c'} \sum_{\mathbf{q},\mathbf{q}'}^{\text{BZ}} X_{v,c,\mathbf{q}}^{(m,\mathbf{Q})} \langle \Psi_0^N | \hat{a}_{j,\tilde{\mathbf{q}}}^\dagger \hat{a}_{c',\mathbf{q}'} \hat{a}_{c,\mathbf{q}+\mathbf{Q}}^\dagger \hat{a}_{v,\mathbf{q}} | \Psi_0^N \rangle \xi_{c',\mathbf{q}'}(\mathbf{r}). \end{aligned} \quad (10)$$

For simplicity, we assumed the ground-state, $|\Psi_0^N\rangle$, to be a single Slater-determinant constructed from the valence states $\phi_{v,\mathbf{q}}$, thereby neglecting the changes in the $N - 1$ electron system upon photoemission. This allows us to work with the $GW + \text{BSE}$ method carried out on top of density functional theory (DFT) calculations, but we stress that our method is also suitable for more general, correlated initial states. The first term in Equation 10 containing the sum over v' then vanishes due to orthogonality of the Bloch states. By the same argument, we can set $c' = c$, $v = j$, $\mathbf{q} = \tilde{\mathbf{q}}$ and $\mathbf{q}' = \mathbf{q} + \mathbf{Q}$ in the remaining term and thus find

$$D_{v,\mathbf{q}}^{(m,\mathbf{Q})}(\mathbf{r}) = \sum_c X_{v,c,\mathbf{q}}^{(m,\mathbf{Q})} \xi_{c,\mathbf{q}+\mathbf{Q}}(\mathbf{r}). \quad (11)$$

Inserting Equation 11 into Equation 7, we get:

$$\left| M_{v,\mathbf{q},\mathbf{k}}^{(m,\mathbf{Q})}(\mathbf{A}) \right| = \left| \int_V d^3r \gamma_{\mathbf{k}}^*(\mathbf{r}) \mathbf{A} \nabla \sum_c X_{v,c,\mathbf{q}}^{(m,\mathbf{Q})} \xi_{c,\mathbf{q}+\mathbf{Q}}(\mathbf{r}) \right| \quad (12)$$

For the photoelectron wave function we follow the commonly applied strategy in POT, namely the plane wave final state (PWFS) approximation: $\gamma_{\mathbf{k}}(\mathbf{r}) = e^{i\mathbf{k}\mathbf{r}}/\sqrt{V}$. Integrating by parts, and dropping the surface term, then allows us to write the matrix element as a sum over Fourier-transformed Bloch functions:

$$\left| M_{v,\mathbf{q},\mathbf{k}}^{(m,\mathbf{Q})}(\mathbf{A}) \right| = \left| \frac{\mathbf{A}\mathbf{k}}{\sqrt{V}} \sum_c X_{v,c,\mathbf{q}}^{(m,\mathbf{Q})} \mathcal{F}[\xi_{c,\mathbf{q}+\mathbf{Q}}](\mathbf{k}) \right| \quad (13)$$

Before putting everything together, we have to take the energy conservation of Equation 3 into account. To this end, we identify the energy of the initial state as the sum of the ground state energy, E_0^N , plus the excitation energy $\Omega^{(m,\mathbf{Q})}$. The energy of the final state consists of the photoelectron kinetic energy, $E_{\text{kin}} = \mathbf{k}^2/2$ and the energy of the $N - 1$ -electron state, $E_{v,\mathbf{q}}^{N-1}$. The latter can

be expressed as the ground-state energy plus the ionization energy of the v -th valence band at \mathbf{q} : $\varepsilon_{v,\mathbf{q}}$. We then obtain

$$\delta(\omega + E_i - E_f) = \delta\left(\omega + \Omega^{(m,\mathbf{Q})} - \varepsilon_{v,\mathbf{q}} - E_{\text{kin}}\right). \quad (14)$$

Combining this expression for the energy conservation with the matrix element of Equation 13, we can now rewrite the transition rate in Equation 3. This rate gives the probability for the m -th exciton, with excitation energy $\Omega^{(m,\mathbf{Q})}$ and center-of-mass momentum \mathbf{Q} , to end up in a state with photoelectron momentum \mathbf{k} , if the photohole resides in valence state $\phi_{v,\mathbf{q}}$:

$$W_{(m,\mathbf{Q}) \rightarrow (v,\mathbf{q},\mathbf{k})} = \frac{2\pi}{V} |\mathbf{A}\mathbf{k}|^2 \left| \sum_c X_{v,c,\mathbf{q}}^{(m,\mathbf{Q})} \mathcal{F}[\xi_{c,\mathbf{q}+\mathbf{Q}}](\mathbf{k}) \right|^2 \cdot \delta\left(\omega + \Omega^{(m,\mathbf{Q})} - \varepsilon_{v,\mathbf{q}} - E_{\text{kin}}\right). \quad (15)$$

Summing up the transition rates for all final-state quantum-numbers v and \mathbf{q} , we get an expression that is proportional to the photoelectron intensity,

$$I_{m,\mathbf{Q}}(\mathbf{k}) \propto |\mathbf{A}\mathbf{k}|^2 \sum_v \sum_{\mathbf{q}}^{\text{BZ}} \left| \sum_c X_{v,c,\mathbf{q}}^{(m,\mathbf{Q})} \mathcal{F}[\xi_{c,\mathbf{q}+\mathbf{Q}}](\mathbf{k}) \right|^2 \cdot \delta\left(\omega + \Omega^{(m,\mathbf{Q})} - \varepsilon_{v,\mathbf{q}} - E_{\text{kin}}\right), \quad (16)$$

where $I_{m,\mathbf{Q}}(\mathbf{k})$ is the experimentally accessible number of photoelectrons of momentum \mathbf{k} , that are emitted from the m -th excited state carrying center-of-mass momentum \mathbf{Q} .

In conclusion, photoemission from a static exciton state is given by a sum over crystal momentum and hole state contributions, for which the photoelectron kinetic energy is given by the energy conservation between the probe-, pump-, and hole energy. At each allowed kinetic energy, the photoelectron angular distribution is given by the absolute squared of a coherent sum over electron contributions, weighted by the respective electron-hole transition coefficients that we obtain from the solutions of the BSE. In contrast to other formulations of exciton photoemission considering that only consider the spectral function, our formalism includes photoelectron matrix element effects due to the probe pulse and at the level of the PWFS approximation.

B. Pump-induced effects on exciton photoemission

In the preceding derivation, we assumed the system was in an *eigenstate* of the BSE Hamiltonian, $|m, \mathbf{Q}\rangle$, whose real-space representation is shown in Equation 1. The resulting expression for the photoelectron intensity (Equation 16) applies to such an eigenstate and does not consider how the system was initially prepared by the pump pulse. In general however, the pump pulse typically generates a *superimposed* state—a linear combination of eigenstates—which necessitates an adaptation of

our formalism, as detailed below. Here, we restrict the discussion to the optical limit ($\mathbf{Q} \rightarrow 0$), allowing us to set $|m, \mathbf{Q} = 0\rangle =: |m\rangle$.

The system's excitation probability due to the pump pulse—characterized by its polarization vector \mathbf{E} and photon energy Ω —is related to the optical spectrum, which is commonly described by the imaginary part of the macroscopic dielectric function [2]:

$$\Im\{\epsilon\}(\Omega) = \frac{16\pi e^2}{\Omega^2} \sum_m |\langle 0 | \mathbf{E} \cdot \hat{\mathbf{v}} | m \rangle|^2 \delta(\Omega - \Omega^{(m)}). \quad (17)$$

Here $|0\rangle$ denotes the ground state, $\hat{\mathbf{v}} = i[\hat{H}, \hat{\mathbf{r}}]$ the single-particle velocity operator and we assume $|\mathbf{E}| = 1$. In the same spirit, we can sum excitons in the energy-degenerate subspace of the BSE Hamiltonian, in order to prepare an initial superimposed state, as created by the pump field. For a small enough energy difference $\eta > 0$, which spans the degenerate subspace around excitation energy Ω_l , we write the superimposed state $|S_l\rangle$ as a linear combination of eigenstates,

$$|S_l\rangle = \sum_m c_m^l |m\rangle, \quad (18)$$

with expansion coefficients c_m^l depending on the polarization of the pump via the optical transition matrix elements:

$$c_m^l = \langle 0 | \mathbf{E} \cdot \hat{\mathbf{v}} | m \rangle \delta\left(|\Omega^{(m)} - \Omega_l| - \eta\right). \quad (19)$$

As a consequence, for photoemission intensity from a superimposed state $|S_l\rangle$ also the transition density matrix elements are changed and thus the final results in Equation 16 must be modified accordingly (for $\mathbf{Q} = 0$):

$$I_{S_l}(\mathbf{k}) \propto |\mathbf{A}\mathbf{k}|^2 \sum_v \sum_{\mathbf{q}}^{\text{BZ}} \left| \sum_m c_m^l X_{v,c,\mathbf{q}}^{(m)} \mathcal{F}[\xi_{c,\mathbf{q}}](\mathbf{k}) \right|^2 \cdot \delta\left(\omega + \Omega_l - \varepsilon_{v,\mathbf{q}} - E_{\text{kin}}\right). \quad (20)$$

In 2D systems excitons typically occur as degenerate pairs, and only their superposition should be considered as the physical exciton, which then, for instance, also respects the symmetries of the system [40, 41]. In contrast to those eigenstates, the pump pulse in general breaks the system's symmetry and may create superimposed exciton states that depend on the pump polarization. As we will show in Paragraph II B, such pump polarization effects have a considerable imprint on exciton photoemission. It should be noted, however, that our formalism is only suitable for degenerate energies (the condition of η being small) and not for the case of a detuned pump pulse, i.e. excitons excited off resonance, and that the above discussion required $\mathbf{Q} = 0$.

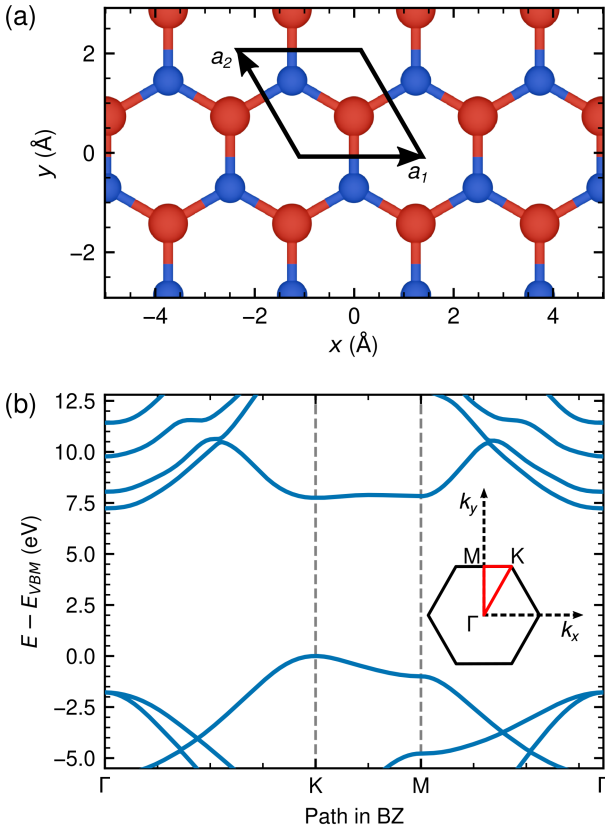


FIG. 1. (a) Atomic structure of hBN. Boron and nitrogen atoms are depicted in red and blue, respectively. The vectors \mathbf{a}_1 and \mathbf{a}_2 span the primitive unit cell, which contains one atom of each kind. (b) G_0W_0 band structure of hBN. Quasiparticle energies are shown along the $\Gamma - K - M - \Gamma$ high symmetry path. The calculated band structure exhibits an indirect band-gap, with the valence-band maximum and conduction-band minimum being located at K (and K') and Γ , respectively.

III. RESULTS

A. Calculation of hBN quasiparticle and optical properties

In the following, we exemplify our formalism by the simulation of excitonic photoemission in monolayer hBN as a prototypical 2D system. As a starting point, we obtain wave functions and energy levels from DFT calculations with QUANTUM ESPRESSO [42–44], using the Perdew-Burke-Ernzerhof (PBE) exchange-correlation functional [45] and a lattice constant of 2.508 \AA , see Figure 1 (a). To compensate for the systematic underestimation of the band gap within semi-local DFT, we apply the G_0W_0 method to correct the energy levels. Utilizing the BERKELEYGW code [1, 2, 46], we obtain a direct (indirect) band gap of 7.6 eV (7.4 eV), which is comparable to literature values from similar methods, see e.g. Ref-

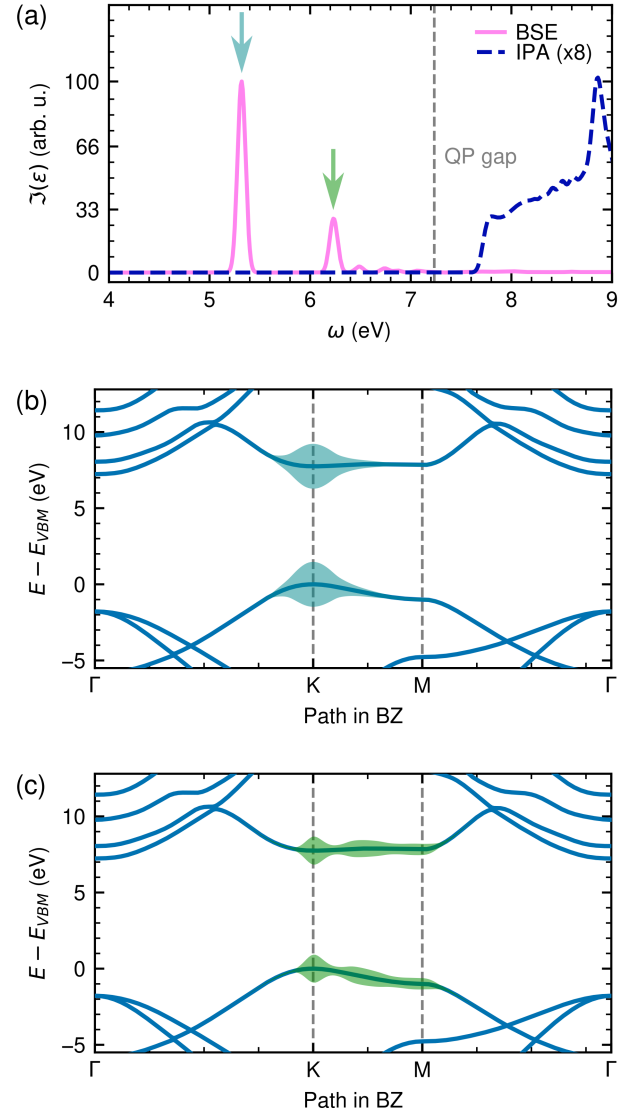


FIG. 2. Optical excitation of monolayer hBN. (a) Independent-particle spectrum, based on a G_0W_0 calculation in dark blue and the BSE spectrum in pink. In the latter, S_1 and S_2 energies are marked by arrows. Panels (b) and (c) show the G_0W_0 band structure with overlays based on the BSE eigenvector composition of the S_1 (blue) and S_2 (green) excitations of the system, respectively.

erence [47] for a comparison. We show the G_0W_0 band structure in Figure 1 (b) and detail the computational methods in Appendix B.

Subsequently, we use the DFT wave functions and G_0W_0 energy levels, and solve the BSE within the TDA and for $\mathbf{Q} = 0$. This yields the excitation energies Ω_m and the BSE eigenvectors $|m, \mathbf{Q} = 0\rangle \equiv |m\rangle$, which we use to simulate optical spectra via Equation 17. As shown in Figure 2 (a), the BSE spectrum features a range of excitonic peaks below the band gap. These are often interpreted as hydrogen-like solutions of the Wannier

equation [48], though they have also been found to deviate from that model [40]. For comparison, we include the optical spectrum computed within the independent-particle approximation (IPA), shown as a dashed blue curve in Figure 2 (a). In the following, we focus on the two lowest excitons, located at 5.3 eV (S_1) and 6.2 eV (S_2).

Both the S_1 and S_2 superimposed excitons are composed of two degenerate eigenstates of the BSE Hamiltonian. This results in an additional dependence on the pump polarization, as discussed in Paragraph II B, and which will become relevant at a later stage in Paragraph III C. For S_1 at 5.3 eV, the two degenerate valence-conduction transitions occur at K and K' , respectively, with their momentum-dependent transition weights indicated in Figure 2 (b). The situation is similar for S_2 at 6.2 eV, albeit with intensities being more spread out along the Brillouin-zone boundary, as can be seen in Figure 2 (c).

B. Exciton photoemission in hBN

With the quasiparticle and optical properties at hand, we now illustrate consequences of our theory for exciton photoemission from monolayer hBN. In the remainder of this manuscript, we use a 26.5 eV probe laser with a Gaussian energy broadening of 0.1 eV. For a better insight into the pump-induced effects on the momentum maps, we ignore the trivial effect of probe polarization, stemming from the $|\mathbf{A}\mathbf{k}|^2$ prefactor in Equation 16. Unlike other theoretical formulations, we only consider excitonic photoemission. As a result, the populated electronic structure and its depopulation due to exciton creation are not accounted for. This is not a significant drawback, since in trARPES experiments the unoccupied part is typically recorded with much lower signal statistics.

In Figure 3 we show the simulated bandmap for photoemission from the S_1 exciton together with the G_0W_0 bandstructure (full blue lines) along the $\Gamma - K' - M_2$ path (corresponding to the k_x -direction, see inset). According to Equation 16, the energy dispersion of exciton photoemission is determined by the hole component of the exciton. Consequently, the exciton's trARPES signature appears at the photoelectron kinetic energy corresponding to the valence band energy plus the pump energy Ω (blue dashed line). This finding, which is well-established in the literature [19, 49], enables the estimation of the exciton's spatial extent from photoemission data under the assumption of an s -like wave function [4, 5, 50].

For this purpose, it is expedient to compare momentum maps of exciton photoemission with those for photoemission from the ground state, which we obtain by the standard way of simulating POT [51]. In Figure 4 (a), we present such a map for a kinetic energy slightly below the valence band maximum (VBM) ($E - E_{VBM} = -0.2$ eV), which is comprised of six triangular features, each around

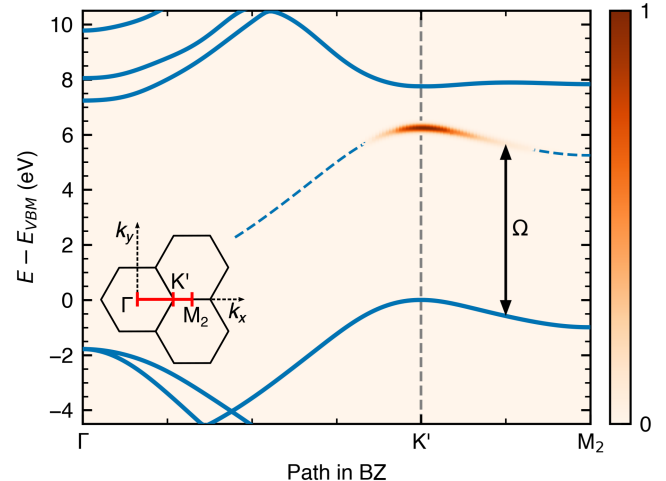


FIG. 3. ARPES bandmap for the S_1 exciton in k_x -direction (cut of the BZ along $\Gamma - K' - M_2$, see inset with three neighboring BZs). The G_0W_0 bandstructure is overlaid in full blue lines, with the valence band, shifted by Ω , indicated in blue dashed lines.

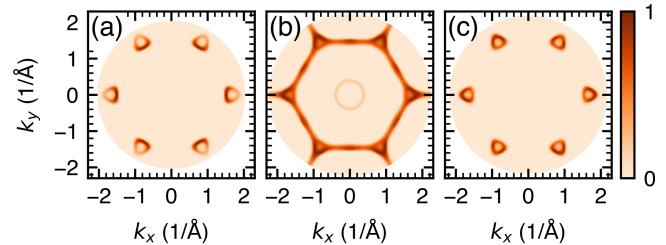


FIG. 4. Momentum maps for three different cases: (a) valence band at $E_b = E_{VBM} - 0.2$ eV ($E_{kin} = 18.6$ eV), (b) conduction band at $E_b = E_{CBM} + 0.6$ eV ($E_{kin} = 26.6$ eV), and (c) S_1 exciton at $E_b = E_{VBM} + \Omega - 0.2$ eV ($E_{kin} = 23.9$ eV).

the K/K' points. This pattern is analogous to the case of graphene, where the triangular features are also broken in the outgoing direction of the Brillouin zone, leading to croissant- or horseshoe-like shapes. This “dark corridor” is due to matrix element effects in the photoemission process and has already been described in great detail for the case of graphene [14, 52, 53]. When assuming a static, charge-transfer induced population of the conduction band, the latter would also be accessible to photoemission from the ground state, which we simulate in panel (b) of Figure 4, using a kinetic energy of 26.6 eV, which is above the conduction band minimum (CBM) ($E - E_{CBM} = +0.6$ eV). In contrast to the valence band case depicted in panel (a), the features around the Dirac point are now elongated in the directions going to the M/M' points, which is reasonable when looking at the bandstructure (see e.g. Figure 3). Remarkably, the dark corridor from the matrix element effect is now pointing to the *inside* of the BZ. Returning now to the simulation of exciton photoemission, we show a momentum map of the S_1 exciton in Figure 4 (c), using a kinetic energy of

23.9 eV and a pump polarization as indicated by a black arrow in Figure 5. As already discussed in the preceding paragraph, the exciton inherits the energy dispersion of the *hole* (here: the highest valence band), but, in light of Equation 16, follows the momentum distribution given by the Fourier-transformed *electron* part of the exciton wave function (here: the lowest conduction band). As a direct imprint of the latter, the dark corridor is also pointing to the inside of the BZ, which we can see clearly in Figure 4 (c). Having established the unoccupied part of the electronic structure as another direct marker of exciton photoemission, we will now examine the different contributions to the momentum maps in more detail.

Using Equation 16, we dissect the photoemission maps for both excitons, S_1 and S_2 , in order to understand the influence of each contributing factor. Since—in this case—both excitons only involve transitions from the highest valence to the lowest conduction band, the sums over v and c in Equation 16 collapse. Consequently, we are left with a single product of $|\mathcal{F}[\xi]|^2$, δ_E and $|X|^2$, involving only wave functions from the lowest conduction band, energies of the highest valence band and BSE transition coefficients from the highest valence band to the lowest conduction band. Figure 5 shows these three factors, as well as the full photoemission maps, for the two excitons in row (a) (S_1) and row (b) (S_2), respectively. The direction of the pump polarization is indicated in the rightmost columns. For both excitons S_1 and S_2 , the triangular patterns are generated by the δ_E factor, with $|\mathcal{F}[\xi]|^2$ only leading to slight modifications. The maps in the first two columns, $|\mathcal{F}[\xi]|^2$ and δ_E , are very similar between the two different excitons S_1 and S_2 , with minor differences arising due to the different photoelectron kinetic energies (23.9 eV for S_1 and 24.8 eV for S_2). Therefore, the additional multiplication with the BSE eigenvector can at most lead to intensity changes within the area of the horseshoes. As can be seen from the third column, the BSE eigenvectors of the two excitons differ, leading to the differences in their respective photoemission maps (rightmost column of Figure 5). In the following, those differences are inspected more closely.

For S_1 in Figure 5 (a), the BSE eigenvector (third column) mostly exhibits a six-fold symmetry. It is centered around the K and K' points and varies weakly along the contours of the horseshoes, thus leading only to small intensity variations along them. Contrary, in the case of S_2 in row (b), the six-fold symmetry is broken by the BSE eigenvector, which exhibits a nodal plane perpendicular to the pump polarization, while being non-zero along the remaining four sides of the hexagonal BZ. Since the pump polarization was chosen along a high-symmetry direction (indicated by black arrows in the rightmost column), it acts as a symmetry axis for the BSE eigenvector and, consequently, for the resulting photoemission map. In contrast to the case of S_1 , the regions around K and K' show much more details for S_2 , particularly featuring nodal lines, which, upon multiplication of the BSE eigenvector with the horseshoe pattern produced by $|\mathcal{F}[\xi]|^2$ and δ_E ,

suppress photoemission intensity. Unlike S_1 , the regions around K and K' for S_2 exhibit more detailed features, including nodal lines, for which photoemission intensity is suppressed in the product of X with the horseshoe pattern produced by $|\mathcal{F}[\xi]|^2$ and δ_E . Moreover, the local maxima are shifted off K and K' . As can be seen in the last column of Figure 5, the combination of all three factors effectively leads to a redistribution of spectral intensity within four out of the six horseshoes. By selectively accessing the different factors in Equation 16, we are thus able to deconvolute different contributions to the momentum maps. In the general case of multiple transitions to an exciton, however, the sums over different valence and conduction bands remain and, as a result, the above analysis would become less straightforward, especially due to the coherent summation of the electron part. Since in the present case of the hBN model we found the most asymmetry arising due to the BSE eigenvectors in conjunction with the pump polarization, we will discuss this effect in more detail in the following.

C. Pump polarization effects in 2D hBN

As outlined in Paragraph II B, the summation of energy-degenerate BSE eigenvectors to form a superimposed exciton involves coefficients that are generally non-unique and depend on the polarization of the pump pulse. The influence of pump polarization is illustrated in detail in Figure 6. Panels (a) and (b) in Figure 6 depict the photoemission from the S_1 exciton (5.3 eV) at a kinetic energy of 23.9 eV and the S_2 exciton (6.2 eV) at 24.8 eV, respectively. The black arrows indicate the polarization direction of the pump-pulse. Photoemission from the first exciton is only weakly dependent on the pump-pulse's polarization and retains the horseshoe intensity pattern. Varying the polarization reveals minor variations in the intensity distributions along the horseshoes. For the second exciton, however, there is a strong dependence of the photoemission intensity distribution on the pump pulse, where different polarizations lead to different redistribution of spectral weight within the horseshoes, allowing for precise control of this redistribution based on the polarization direction. Although the probe pulse polarization may introduce an overall attenuation in an trARPES experiment, pump-induced effects on exciton photoemission are expected to be observable, provided that sufficient energy and momentum resolution are achieved.

IV. CONCLUSIONS

We have developed a framework for exciton photoemission orbital tomography (exPOT) in periodic systems, thereby enabling the computation and interpretation of photoemission angular distributions from excitons in crystalline two-dimensional materials. The ex-

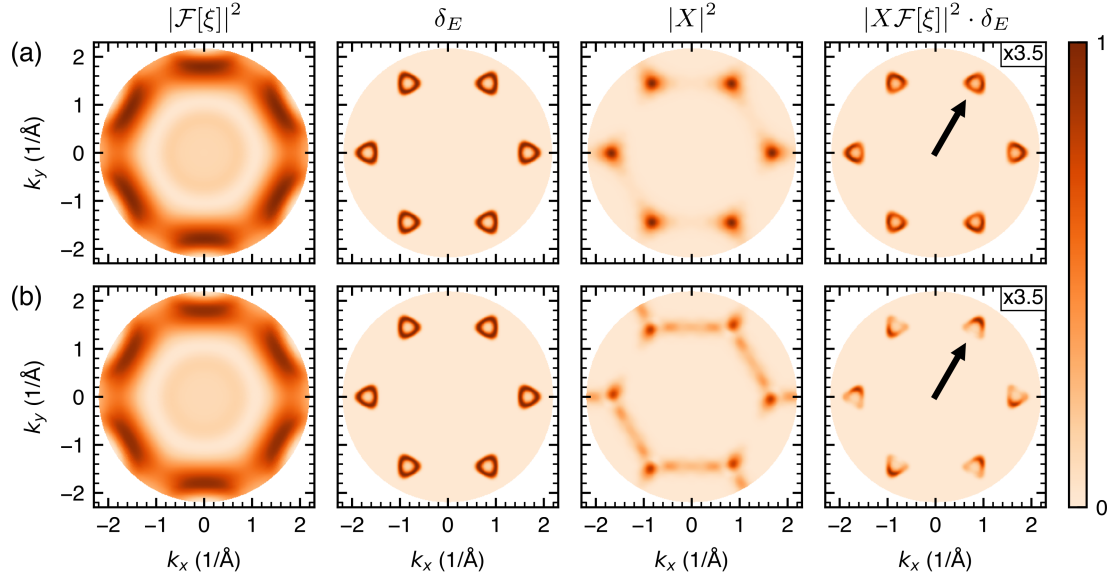


FIG. 5. Decomposition of exciton ARPES maps for S_1 in row (a) and S_2 in row (b), with black arrows indicating the polarization of the pump laser. First column: Fourier-transformed conduction-band wave functions. Second column: energy-conservation delta-function. Third column: BSE eigenvectors. Fourth column: resulting exciton ARPES maps as products of first to third columns. Each map is individually normalized to one. For S_1 in row (a), the horseshoes point away from Γ , with minor modulations along their contours. For S_2 in row (b), four of the six horseshoes are rotated, when compared to the first exciton. This is a direct result of the differences in the momentum-space distribution of their BSE eigenvectors.

POT formalism is derived from first principles, using many-body perturbation theory and the Dyson orbital concept, and connects the photoemission intensity to results from GW +BSE calculations. As a manifestation of the electron-hole correlation, for each hole configuration, exciton photoemission is expressed as a coherent sum over Fourier-transformed conduction-band wave functions, weighted by the Bethe-Salpeter eigenvectors.

We have implemented the formalism in a computational workflow compatible with standard plane wave basis set GW +BSE, using DFT wave functions, GW energies, and BSE eigenvectors. As a proof of concept, we have applied our formalism to the prototypical case of monolayer hexagonal boron nitride. The resulting exPOT maps exhibit distinct patterns for different excitonic states. These patterns are characterized by an energy dispersion that follows the hole states, while the electron part of the exciton wave function is reflected in the photoemission matrix element. Both contributions are further modified by the BSE eigenvectors. The latter introduces an additional dependence on the pump polarization, resulting in the suppression of spectral weight in the momentum maps as a direct consequence of the excitonic character.

The exPOT formalism for periodic systems bridges the gap between ab-initio many-body theory and experimentally measurable momentum-resolved spectra of excitons. It provides a powerful tool for gaining microscopic insight into the internal structure of excitons and offers a predictive framework for designing and inter-

preting next-generation trARPES experiments on low-dimensional quantum materials. Our formalism also includes excitons with finite center-of-mass momentum, making it particularly suited for elucidating the nature of momentum-dark excitons by establishing a direct connection between theory and experiment.

Appendix A: Expansion of Dyson orbitals in Bloch states

In this section, we derive the expansion in Equation 9 of the Dyson orbitals, as described in Equation 8, into Bloch functions.

Since this expansion holds in general, we start with the Dyson orbital formed by the overlap of an arbitrary $N-1$ - and N -electron wave function:

$$D(\mathbf{r}) = \sqrt{N} \int_V d^3r_2 \dots d^3r_N \Psi^{N-1}(\mathbf{r}_2, \dots, \mathbf{r}_N)^* \Psi^N(\mathbf{r}, \mathbf{r}_2, \dots, \mathbf{r}_N) \quad (A1)$$

Next, since the Dyson orbitals are one-electron wave functions, they can be expanded in any set of one-electron basis functions. For a set of (BvK-periodic, just like D) orthonormal basis functions $\{\psi_j(\cdot)\}$ we can thus write

$$D(\mathbf{r}) = \sum_j c_j \psi_j(\mathbf{r}), \quad (A2)$$

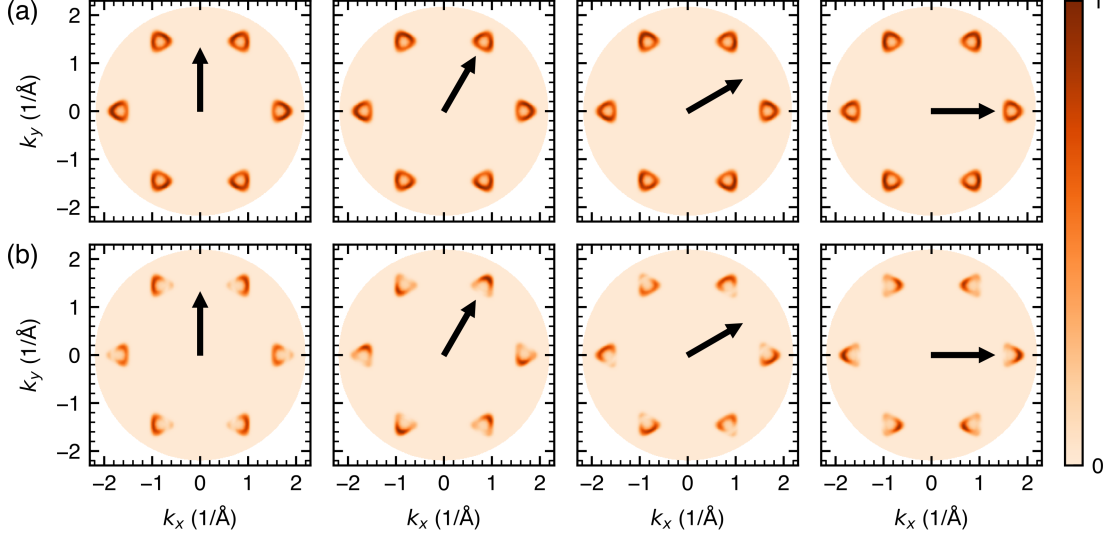


FIG. 6. Influence of pump laser's polarization on exciton photoemission. The four columns shows ARPES photoemission maps for different polarizations of the pump laser (black arrows). (a) shows photoemission from the lowest-energy exciton while (b) shows the second exciton. In the case of the first exciton, only small differences in the intensity distribution along the horseshoes is visible, while for the second exciton, there is a strong dependence on the pump polarization. Different polarizations lead to different rotations of the horseshoes. In the case of both excitons, the photoemission maps are mirror symmetric across the (high-symmetry) polarization directions.

with linear coefficients

$$c_j = \int_V d^3r \psi_j(\mathbf{r})^* D(\mathbf{r}). \quad (\text{A3})$$

Inserting the Dyson orbital and renaming \mathbf{r} to \mathbf{r}_1 , we get

$$c_j = \sqrt{N} \int_V d^3r_1 d^3r_2 \dots d^3r_N \psi_j(\mathbf{r}_1)^* \Psi^{N-1}(\mathbf{r}_2, \dots, \mathbf{r}_N)^* \Psi^N(\mathbf{r}_1, \mathbf{r}_2, \dots, \mathbf{r}_N). \quad (\text{A4})$$

Next, we rename \mathbf{r}_1 to \mathbf{r}_2 and vice versa to get

$$\begin{aligned} c_j &= \sqrt{N} \int_V d^3r_1 d^3r_2 \dots d^3r_N \psi_j(\mathbf{r}_2)^* \Psi^{N-1}(\mathbf{r}_1, \mathbf{r}_3, \dots, \mathbf{r}_N)^* \Psi^N(\mathbf{r}_2, \mathbf{r}_1, \dots, \mathbf{r}_N) \\ &= \sqrt{N} \int_V d^3r_1 d^3r_2 \dots d^3r_N \psi_j(\mathbf{r}_2)^* \Psi^{N-1}(\mathbf{r}_1, \mathbf{r}_3, \dots, \mathbf{r}_N)^* (-\Psi^N(\mathbf{r}_1, \mathbf{r}_2, \dots, \mathbf{r}_N)), \end{aligned} \quad (\text{A5})$$

where we used the Pauli exclusion principle in the last step.

Using the same argument, we find for any i in $\{1, \dots, N\}$:

$$\begin{aligned} c_j &= \sqrt{N} \int_V d^3r_1 \dots d^3r_N (-1)^{1+i} \psi_j(\mathbf{r}_i)^* \Psi^{N-1}(\mathbf{r}_1, \dots, \mathbf{r}_{i-1}, \mathbf{r}_{i+1}, \dots, \mathbf{r}_N)^* \Psi^N(\mathbf{r}_1, \mathbf{r}_2, \dots, \mathbf{r}_N) \end{aligned} \quad (\text{A6})$$

We can thus write c_j as a sum over i as:

$$\begin{aligned} c_j &= \frac{1}{N} \sum_{i=1}^N \sqrt{N} \int_V d^3r_1 \dots d^3r_N (-1)^{1+i} \psi_j(\mathbf{r}_i)^* \Psi^{N-1}(\mathbf{r}_1, \dots, \mathbf{r}_{i-1}, \mathbf{r}_{i+1}, \dots, \mathbf{r}_N)^* \Psi^N(\mathbf{r}_1, \dots, \mathbf{r}_N) \\ &= \int_V d^3r_1 \dots d^3r_N \Psi^N(\mathbf{r}_1, \dots, \mathbf{r}_N) \\ &\quad \cdot \left(\sum_{i=1}^N \frac{(-1)^{1+i}}{\sqrt{N}} \psi_j(\mathbf{r}_i) \Psi^{N-1}(\mathbf{r}_1, \dots, \mathbf{r}_{i-1}, \mathbf{r}_{i+1}, \dots, \mathbf{r}_N) \right)^* \end{aligned} \quad (\text{A7})$$

Now, note, that the expression in parenthesis is precisely the antisymmetrized product $|\mathcal{A}\psi_j\Psi^{N-1}\rangle$ (see, e.g., [37]). Using the creation operator \hat{a}_j^\dagger corresponding to $|\psi_j\rangle$ and a bra-ket notation, we can thus write

$$\begin{aligned} c_j &= \int_V d^3r_1 \dots d^3r_N \langle \mathbf{r}_1, \dots, \mathbf{r}_N | \Psi^N \rangle \\ &\quad \left(\langle \mathbf{r}_1, \dots, \mathbf{r}_N | \hat{a}_j^\dagger | \Psi^{N-1} \rangle \right)^* \\ &= \int_V d^3r_1 \dots d^3r_N \langle \Psi^{N-1} | \hat{a}_j | \mathbf{r}_1, \dots, \mathbf{r}_N \rangle \langle \mathbf{r}_1, \dots, \mathbf{r}_N | \Psi^N \rangle. \end{aligned} \quad (\text{A8})$$

Finally, we want to arrive at a basis-independent representation of c_j , which allows for efficient handling of the ladder-operator matrix-elements. To do so, we make use of the fact, that for every wave function $\Psi(\cdot)$, that satisfies BvK periodic boundary conditions for a large

crystal, there is a non-periodic wave function $\tilde{\Psi}(\cdot)$, that is equal to $\Psi(\cdot)$ inside the crystal, but vanishes quickly outside of the crystal. Then, we get

$$\begin{aligned} c_j &= \int_V d^3r_1 \dots d^3r_N \langle \Psi^{N-1} | \hat{a}_j | \mathbf{r}_1, \dots, \mathbf{r}_N \rangle \langle \mathbf{r}_1, \dots, \mathbf{r}_N | \Psi^N \rangle \\ &\approx \int_V d^3r_1 \dots d^3r_N \langle \tilde{\Psi}^{N-1} | \hat{a}_j | \mathbf{r}_1, \dots, \mathbf{r}_N \rangle \langle \mathbf{r}_1, \dots, \mathbf{r}_N | \tilde{\Psi}^N \rangle, \end{aligned} \quad (\text{A9})$$

where \hat{a}_j is the destruction operator for $|\tilde{\psi}_j\rangle$, which is the non-periodic equivalent of basis vector $|\psi_j\rangle$. Assuming the non-periodic functions vanish quickly outside of V , we then get

$$\begin{aligned} c_j &\approx \int_{\mathbb{R}^3} d^3r_1 \dots d^3r_N \langle \tilde{\Psi}^{N-1} | \hat{a}_j | \mathbf{r}_1, \dots, \mathbf{r}_N \rangle \langle \mathbf{r}_1, \dots, \mathbf{r}_N | \tilde{\Psi}^N \rangle \\ &= \langle \tilde{\Psi}^{N-1} | \hat{a}_j | \tilde{\Psi}^N \rangle, \end{aligned} \quad (\text{A10})$$

where we used

$$\hat{\mathbb{1}} = \int_{\mathbb{R}^3} d^3r | \mathbf{r} \rangle \langle \mathbf{r} |. \quad (\text{A11})$$

We can thus perform operations in a basis-independent manner using the non-periodic wave functions and then transform back to the BvK wave functions. Symbolically, we can thus simply write

$$c_j = \langle \Psi^{N-1} | \hat{a}_j | \Psi^N \rangle \quad (\text{A12})$$

as a shorthand for the above-shown steps.

Inserting this into Equation A2, we get our final result for the expansion of the Dyson orbital D in an arbitrary, orthonormal basis set $\{\psi_j(\cdot)\}$:

$$D(\mathbf{r}) = \sum_j \langle \Psi^{N-1} | \hat{a}_j | \Psi^N \rangle \psi_j(\mathbf{r}) \quad (\text{A13})$$

To get to Equation 9, we then simply use the Bloch functions as basis functions and split the sum over bands into a sum over valence bands and a sum over conduction bands.

Appendix B: Computational Details

For the example of monolayer hBN, we calculate Kohn-Sham DFT wave functions and energies in QUANTUM ESPRESSO [42–44] using the PBE exchange-correlation functional, ONCV pseudopotentials and a cutoff energy of 50 Ry and 200 Ry for the wave functions and the representation of the density, respectively. The lattice constant was set to 2.507 Å (bulk experimental value: 2.506 Å [54]) and we use a vacuum layer of 20 Å, as well as a truncation of the Coulomb interaction in z -direction [55], in order to avoid spurious interaction between repeated slabs from the periodic boundary condition. Based on these ground-state properties, we perform a G_0W_0 calculation using BERKELEYGW [1, 2, 46]. In particular, we use the *NNS* subsampling technique, which, for systems with reduced dimensionality, accelerates convergence with respect to the Brillouin zone sampling [56]. For the calculation of the static inverse dielectric function we use a 12x12x1 sampling of the Brillouin zone, a cutoff energy of 30 Ry for reciprocal lattice vectors and sum over 200 bands. Based on this, we calculate the G_0W_0 energies for 4 valence and 44 conduction bands, using the same k-space mesh and reciprocal lattice cutoff as for the inverse dielectric function.

Finally, we construct the BSE Hamiltonian using 4 valence and 9 conduction bands on a 12x12x1 k-space mesh, interpolate it to a 96x96x1 k-space mesh (4 valence, 4 conduction bands) and diagonalize the BSE Hamiltonian.

[1] M. S. Hybertsen and S. G. Louie, Phys. Rev. B **34**, 5390 (1986).

[2] M. Rohlffing and S. G. Louie, Phys. Rev. B **62**, 4927 (2000).

[3] G. Onida, L. Reining, and A. Rubio, Rev. Mod. Phys. **74**, 601 (2002).

[4] J. Madéo, M. K. L. Man, C. Sahoo, M. Campbell, V. Pareek, E. L. Wong, A. Al-Mahboob, N. S. Chan, A. Karmakar, B. M. K. Mariserla, X. Li, T. F. Heinz, T. Cao, and K. M. Dani, Science **370**, 1199 (2020).

[5] M. K. L. Man, J. Madéo, C. Sahoo, K. Xie, M. Campbell, V. Pareek, A. Karmakar, E. L. Wong, A. Al-Mahboob, N. S. Chan, D. R. Bacon, X. Zhu, M. M. M. Abdelrasoul, X. Li, T. F. Heinz, F. H. da Jornada, T. Cao, and K. M. Dani, Science Advances **7**, eabg0192 (2021), <https://www.science.org/doi/pdf/10.1126/sciadv.abg0192>.

[6] S. Dong, M. Puppin, T. Pincelli, S. Beaulieu, D. Christiansen, H. Hübener, C. Nicholson, R. Xian, M. Dendzik, Y. Deng, Y. Windsor, M. Selig, E. Malic, A. Rubio, A. Knorr, M. Wolf, L. Rettig, and R. Ernstorfer, Natural Sciences **1** (2021).

[7] R. Wallauer, M. Raths, K. Stallberg, L. Münster, D. Brandstetter, X. Yang, J. Gütte, P. Puschnig, S. Soubatch, C. Kumpf, F. C. Bocquet, F. S. Tautz, and U. Höfer, Science **371**, 1056 (2021).

[8] R. Wallauer, R. Perea-Causin, L. Münster, S. Zajusch, S. Brem, J. Gütte, K. Tanimura, K.-Q. Lin, R. Huber, E. Malic, and U. Höfer, Nano Letters **21**, 5867 (2021).

[9] W. Bennecke, A. Windischbacher, D. Schmitt, J. P. Bange, R. Hemm, C. S. Kern, G. D'Avino, X. Blase, D. Steil, S. Steil, M. Aeschlimann, B. Stadtmüller, M. Reutzel, P. Puschnig, G. S. M. Jansen, and S. Mathias, Nature Communications **15**, 1804 (2024).

[10] M. Reutzel, G. S. M. Jansen, and S. Mathias, Advances in Physics: X **9**, 2378722 (2024).

[11] M. Dauth and S. Kümmel, Phys. Rev. A **93**, 022502

(2016).

[12] U. De Giovannini, H. Hübener, and A. Rubio, *J. Chem. Theory Comput.* **13**, 265 (2017).

[13] M. Dauth, M. Graus, I. Schelter, M. Wießner, A. Schöll, F. Reinert, and S. Kümmel, *Phys. Rev. Lett.* **117**, 183001 (2016).

[14] C. S. Kern, A. Haags, L. Egger, X. Yang, H. Kirschner, S. Wolff, T. Seyller, A. Gottwald, M. Richter, U. De Giovannini, A. Rubio, M. G. Ramsey, F. C. Bocquet, S. Soubatch, F. S. Tautz, P. Puschnig, and S. Moser, *Phys. Rev. Research* **5**, 033075 (2023).

[15] G. Stefanucci and R. van Leeuwen, *Nonequilibrium Many-Body Theory of Quantum Systems: A Modern Introduction*, 2nd ed. (Cambridge University Press, 2025).

[16] J. K. Freericks, H. R. Krishnamurthy, and T. Pruschke, *Phys. Rev. Lett.* **102**, 136401 (2009).

[17] E. Perfetto, D. Sangalli, A. Marini, and G. Stefanucci, *Phys. Rev. B* **94**, 245303 (2016).

[18] M. Schüller and M. A. Sentef, *Journal of Electron Spectroscopy and Related Phenomena* **253**, 147121 (2021).

[19] A. Rustagi and A. F. Kemper, *Phys. Rev. B* **97**, 235310 (2018).

[20] D. Sangalli, *Phys. Rev. Mater.* **5**, 083803 (2021).

[21] P. Törmä, *Phys. Rev. Lett.* **131**, 240001 (2023).

[22] M. Kang, S. Kim, Y. Qian, P. M. Neves, L. Ye, J. Jung, D. Puntel, F. Mazzola, S. Fang, C. Jozwiak, A. Bostwick, E. Rotenberg, J. Fuji, I. Vobornik, J.-H. Park, J. G. Checkelsky, B.-J. Yang, and R. Comin, *Nature Physics* **21**, 110 (2025).

[23] S. Cho, J.-H. Park, J. Hong, J. Jung, B. S. Kim, G. Han, W. Kyung, Y. Kim, S.-K. Mo, J. D. Denlinger, J. H. Shim, J. H. Han, C. Kim, and S. R. Park, *Phys. Rev. Lett.* **121**, 186401 (2018).

[24] M. Schüller, U. D. Giovannini, H. Hübener, A. Rubio, M. A. Sentef, and P. Werner, *Science Advances* **6**, eaay2730 (2020).

[25] M. Ünzelmann, H. Bentmann, T. Figgemeier, P. Eck, J. N. Neu, B. Geldiyyev, F. Diekmann, S. Rohlf, J. Buck, M. Hoesch, M. Kalläne, K. Rossnagel, R. Thomale, T. Siegrist, G. Sangiovanni, D. D. Sante, and F. Reinert, *Nature Communications* **12**, 3650 (2021).

[26] M. Schüller, U. De Giovannini, H. Hübener, A. Rubio, M. A. Sentef, T. P. Devereaux, and P. Werner, *Phys. Rev. X* **10**, 041013 (2020).

[27] I. Adawi, *Phys. Rev.* **134**, A788 (1964).

[28] P. J. Feibelman and D. E. Eastman, *Phys. Rev. B* **10**, 4932 (1974).

[29] P. Puschnig, S. Berkebile, A. J. Fleming, G. Koller, K. Emtsev, T. Seyller, J. D. Riley, C. Ambrosch-Draxl, F. P. Netzer, and M. G. Ramsey, *Science* **326**, 702 (2009).

[30] C. S. Kern, A. Windischbacher, and P. Puschnig, *Phys. Rev. B* **108**, 085132 (2023).

[31] Z. Ye, T. Cao, K. O'Brien, H. Zhu, X. Yin, Y. Wang, S. G. Louie, and X. Zhang, *Nature* **513**, 214 (2014).

[32] F. Wu, F. Qu, and A. H. MacDonald, *Phys. Rev. B* **91**, 075310 (2015).

[33] C. Poellmann, P. Steinleitner, U. Leierseder, P. Nagler, G. Plechinger, M. Porer, R. Bratschitsch, C. Schüller, T. Korn, and R. Huber, *Nature Materials* **14**, 889 (2015).

[34] D. Sangalli, E. Perfetto, G. Stefanucci, and A. Marini, *The European Physical Journal B* **91**, 171 (2018).

[35] A. Marini, E. Perfetto, and G. Stefanucci, *Journal of Electron Spectroscopy and Related Phenomena* **257**, 147189 (2022).

[36] A. Damascelli, *Phys. Scr.* **T109**, 61 (2004).

[37] M. Dauth, M. Wiessner, V. Feyer, A. Schöll, P. Puschnig, F. Reinert, and S. Kümmel, *New J. Phys.* **16**, 103005 (2014).

[38] D. G. Truhlar, P. C. Hiberty, S. Shaik, M. S. Gordon, and D. Danovich, *Angewandte Chemie* **131**, 12460 (2019).

[39] A. I. Krylov, *J. Chem. Phys.* **153**, 080901 (2020).

[40] T. Galvani, F. Paleari, H. P. C. Miranda, A. Molina-Sánchez, L. Wirtz, S. Latil, H. Amara, and F. m. c. Ducastelle, *Phys. Rev. B* **94**, 125303 (2016).

[41] A. J. Uría-Álvarez, J. J. Esteve-Paredes, M. García-Blázquez, and J. J. Palacios, *Computer Physics Communications* **295**, 109001 (2024).

[42] P. Giannozzi, S. Baroni, N. Bonini, M. Calandra, R. Car, C. Cavazzoni, D. Ceresoli, G. L. Chiarotti, M. Cococcioni, I. Dabo, A. D. Corso, S. de Gironcoli, S. Fabris, G. Fratesi, R. Gebauer, U. Gerstmann, C. Gougoassis, A. Kokalj, M. Lazzeri, L. Martin-Samos, N. Marzari, F. Mauri, R. Mazzarello, S. Paolini, A. Pasquarello, L. Paulatto, C. Sbraccia, S. Scandolo, G. Sclauzero, A. P. Seitsonen, A. Smogunov, P. Umari, and R. M. Wentzcovitch, *J. Phys. Condens Matter* **21**, 395502 (2009).

[43] P. Giannozzi, O. Andreussi, T. Brumme, O. Bunau, M. B. Nardelli, M. Calandra, R. Car, C. Cavazzoni, D. Ceresoli, M. Cococcioni, N. Colonna, I. Carnimeo, A. D. Corso, S. de Gironcoli, P. Delugas, R. A. DiStasio, A. Ferretti, A. Floris, G. Fratesi, G. Fugallo, R. Gebauer, U. Gerstmann, F. Giustino, T. Gorni, J. Jia, M. Kawamura, H.-Y. Ko, A. Kokalj, E. Küçükbenli, M. Lazzeri, M. Marsili, N. Marzari, F. Mauri, N. L. Nguyen, H.-V. Nguyen, A. O. de-la Roza, L. Paulatto, S. Poncé, D. Rocca, R. Sabatini, B. Santra, M. Schlipf, A. P. Seitsonen, A. Smogunov, I. Timrov, T. Thonhauser, P. Umari, N. Vast, X. Wu, and S. Baroni, *Journal of Physics: Condensed Matter* **29**, 465901 (2017).

[44] P. Giannozzi, O. Baseggio, P. Bonfà, D. Brunato, R. Car, I. Carnimeo, C. Cavazzoni, S. de Gironcoli, P. Delugas, F. Ferrari Ruffino, A. Ferretti, N. Marzari, I. Timrov, A. Urru, and S. Baroni, *The Journal of Chemical Physics* **152**, 154105 (2020), https://pubs.aip.org/aip/jcp/article-pdf/doi/10.1063/5.0005082/16721881/154105_1.online.pdf.

[45] J. P. Perdew, K. Burke, and M. Ernzerhof, *Phys. Rev. Lett.* **77**, 3865 (1996).

[46] J. Deslippe, G. Samsonidze, D. A. Strubbe, M. Jain, M. L. Cohen, and S. G. Louie, *Computer Physics Communications* **183**, 1269 (2012).

[47] A. Kirchhoff, T. Deilmann, P. Krüger, and M. Rohlfing, *Phys. Rev. B* **106**, 045118 (2022).

[48] G. H. Wannier, *Physical Review* **52**, 191 (1937).

[49] M. Weinelt, M. Kutschera, T. Fauster, and M. Rohlfing, *Phys. Rev. Lett.* **92**, 126801 (2004).

[50] O. Karni, E. Barré, V. Pareek, J. D. Georgaras, M. K. L. Man, C. Sahoo, D. R. Bacon, X. Zhu, H. B. Ribeiro, A. L. O'Beirne, J. Hu, A. Al-Mahboob, M. M. M. Abdelrasoul, N. S. Chan, A. Karmakar, A. J. Winchester, B. Kim, K. Watanabe, T. Taniguchi, K. Barmak, J. Madéo, F. H. da Jornada, T. F. Heinz, and K. M. Dani, *Nature* **603**, 247 (2022).

[51] D. Lüftner, S. Weiß, X. Yang, P. Hurdax, V. Feyer, A. Gottwald, G. Koller, S. Soubatch, P. Puschnig, M. G. Ramsey, and F. S. S. Tautz, *Phys. Rev. B* **96**, 125402

(2017).

- [52] I. Gierz, J. Henk, H. Höchst, C. R. Ast, and K. Kern, Phys. Rev. B **83**, 121408 (2011).
- [53] E. Krasovskii, Nanomaterials **11**, 10.3390/nano11051212 (2021).
- [54] A. Bosak, J. Serrano, M. Krisch, K. Watanabe, T. Taniguchi, and H. Kanda, Phys. Rev. B **73**, 041402 (2006).
- [55] T. Sohier, M. Calandra, and F. Mauri, Phys. Rev. B **96**, 075448 (2017).
- [56] F. H. da Jornada, D. Y. Qiu, and S. G. Louie, Physical Review B **95**, 035109 (2017).